Materials Advances

ROYAL SOCIETY OF CHEMISTRY

PAPER

View Article Online
View Journal

Cite this: DOI: 10.1039/d6ma00048g

Synthesis and morphology control of SbSeI thin films at elevated pressure

Alejandro Navarro-Güell, *[ab] Ivan Caño, [ab] David Rovira, [ab] Alex Jimenez-Arguijo, [ab] Gabriel Aygur, [c] Joaquim Puigdollers, [ab] Joel van Embden[c] and Edgardo Saucedo [ab]

SbSeI is a promising quasi-one-dimensional chalcohalide for optoelectronic applications, but its strong tendency to form needle-like structures makes thin-film morphology difficult to control. Here, we investigate the temperature- and time-dependent evolution of SbSeI formed by the reaction of Sb_2Se_3 thin films with SbI_3 vapour under elevated pressure. Systematic SEM, XRD, and cross-sectional EDS analyses reveal two distinct growth regimes. At low temperature, incomplete conversion and limited lateral mass transport yield dense, thin needles and thickness distributions that evolve towards Weibull-like behaviour. At higher temperatures, conversion occurs largely during the heating ramp, resulting in the formation of a continuous SbSeI-rich underlayer, and subsequent mass redistribution promotes thicker needles with lognormal thickness statistics. These results support a two-interface growth mechanism in which the accessibility of iodine-rich species and thermally activated surface mass transport together govern the transition from thin to thick needles. These findings provide practical guidelines for tuning the temperature, time, and pressure to engineer the morphology of SbSeI films and offer a mechanistic framework that may be transferable to other quasi-one-dimensional chalcohalides governed by anisotropic growth.

Received 9th January 2026,
Accepted 7th May 2026

DOI: 10.1039/d6ma00048g

rsc.li/materials-advances

1. Introduction

van der Waals (vdW) chalcogenides are an emerging class of materials that have attracted growing attention due to their promising properties for applications in photovoltaics, photodetection, photoelectrochemistry, and sensing.[1–5] These materials are characterized by strong covalent bonding along one or more crystallographic directions, with the remaining directions held together by weaker vdW interactions. This structural anisotropy results in direction-dependent properties, such as enhanced carrier mobility and thermal conductivity along the covalently bonded axes. Such anisotropy is common to other well-known (layered) 2D materials, such as MoS_2, $MoSe_2$, and WS_2.[6,7]

Among these materials, those with covalent bonding along a single crystallographic direction, such as Sb_2Se_3 and Sb_2S_3, are referred to as quasi-one-dimensional (Q-1D) materials. Recent research has demonstrated their potential as absorber layers within solar cells and highlighted the importance of orientation-engineering strategies to achieve power conversion efficiencies above 10%.[8–12] A promising approach to expand the chemical tunability and functional versatility of these Q-1D materials involves substituting one chalcogen atom (oxidation state −2) in the binary compound with two halogen atoms (oxidation state −1) to form a ternary chalcohalide compound. This family of materials has the general formula MChX (where M = Sb, Bi; Ch = Se, S; X = Br, I) and shows band gaps ranging from 1.2 to 2.2 eV, high optical absorption coefficients, and excellent environmental stability.[13–15]

At present, a major challenge to the further development of chalcohalide materials is the inability to adequately control their thin-film morphology. Their inherently anisotropic crystal structure strongly favours the formation of needle or rod-like structures. While there have been many attempts to fabricate compact thin films, none have succeeded in producing films of sufficient quality for subsequent integration into optoelectronic devices (solar cells, sensors, and electrodes) with conventional planar architectures.

Antimony selenoiodide (SbSeI) is a promising chalcohalide semiconductor that meets key criteria for optoelectronic applications, including a suitable bandgap of 1.69 eV, strong optical absorption ($\sim 10^5 cm^{-1}$), and low carrier effective masses.[4,13,16] In addition, SbSeI exhibits a high dielectric constant, which is known to favour long carrier lifetimes, large diffusion lengths

[a] Photovoltaic Lab-Micro and Nano Technologies Group (MNT), Electronic Engineering Department, Universitat Politècnica de Catalunya (UPC), Barcelona 08026, Spain. E-mail: alejandro.navarro.guell@upc.edu
[b] Barcelona Center for Multiscale Science & Engineering, Barcelona 08026, Spain
[c] School of Science, RMIT University, Victoria 3001, Australia

and high mobility–lifetime product ($\mu\tau$) values.[17] Structurally, SbSeI consists of quasi-one-dimensional chains, and thin films therefore form needle-like crystallites that are several micrometers long and only a few hundred nanometres in diameter, typically with random orientation relative to the substrate. The strong thermodynamic driving force for needle formation makes it challenging to identify synthesis conditions that provide good control over both morphology and crystallographic orientation. Therefore, detailed investigations to understand the growth mechanism are essential to rationally tailor SbSeI films suitable for high-performing optoelectronic applications.

Several synthetic strategies have been reported for the fabrication of SbSeI. Nowak *et al.* employed sonochemical techniques to produce nanowires and observed a preferred growth direction along [001] over [110].[18] Wibowo *et al.* synthesized single crystals using the vertical Bridgman growth method, reporting intrinsic n-type behaviour and comparable electron and hole $\mu\tau$ ($\sim 10^{-4}$ cm^2 V^{-1}), comparable to those of leading semiconductor detector materials.[17] Further work has explored spin-coating and annealing approaches using molecular inks, demonstrating the potential for one-step deposition.[19] Balakrishnan *et al.* proposed a topotactic transformation mechanism from Sb_2Se_3 needles to SbSeI needles, contributing valuable insight, however, without achieving morphological control.[20] Dolcet *et al.* reported the formation of vertically aligned SbSeI films *via* reactive annealing of Sb_2Se_3 in a sealed quartz ampoule under SbI_3 vapor and analysed the influence of synthesis parameters but stopping short of a mechanistic explanation.[21] More recently, R. Nie *et al.* demonstrated the photovoltaic potential of SbSeI using a two-step spin-coating method. The authors circumvented the morphological challenges by generating SbSeI within a mesoporous TiO_2 matrix. They achieved a solar cell power conversion efficiency of 4.1% and reported excellent thermal, moisture, and photostability.[22] Finally, our group has demonstrated the viability of synthesizing this compound and related members of the family using both PVD-based processes and purely chemical routes, underscoring the versatility of these materials.[13,14] Despite these excellent advances in synthetic methods and applications, a detailed understanding of the needle-growth mechanism and the influence of synthesis parameters on film morphology remains lacking.

Here, we investigate the morphological and structural evolution of SbSeI films synthesized *via* reactive annealing, in which Sb_2Se_3 films are exposed to SbI_3 vapor within a semi-confined environment under elevated pressure. Operating at elevated pressures ($\gg$1 atm) prevents the rapid loss of SbI_3 and enables controlled SbSeI formation. This high-pressure approach has been barely explored in the context of SbSeI synthesis and enables a systematic study of the transformation pathways governing film morphology and crystal structure. To probe these pathways, we conduct time-resolved annealing experiments across a range of temperature regimes. The resulting films are characterized at each stage using scanning electron microscopy (SEM) and X-ray diffraction (XRD). Detailed analyses, including texture coefficient (TC) calculations, microstructural examination, and the application of diffusion-based crystal growth theory, allow us to propose a reaction mechanism linking processing conditions to the morphology and crystal structure.

Previous studies have already established pressure-assisted synthesis routes for SbSeI and related chalcohalides, as well as parameter-dependent preparation of SbSeI thin films. The aim of the present work is therefore not to introduce a fundamentally new synthesis route, but to resolve how temperature, time, and pressure influence phase evolution and morphology during reactive annealing. By combining SEM, XRD, and cross-sectional EDS, we identify distinct low- and high-temperature growth regimes and propose a cautious mechanistic interpretation linking conversion, underlayer formation, and subsequent needle thickening.

2. Experimental section

2.1. Materials and precursor film deposition

Antimony selenide (Sb_2Se_3) precursor films were deposited onto commercially available 2.5 $\times$ 2.5 cm^2 FTO (TEC 15) substrates, coated with a compact TiO_2 layer. TiO_2 typically serves as an electron transport layer (ETL) in many devices. The fabricated (superstrate) architecture was selected to ensure compatibility with future integration into functional optoelectronic devices.

Substrates were first cleaned using a sequential protocol consisting of (1) mechanical scrubbing with Liquinox detergent, (2) 10 minutes in an ultrasonic bath with isopropanol, (3) 10 minutes in Milli-Q water, and (4) 10 minutes of UV-O_3 surface treatment. The TiO_2 (35 nm) layer was deposited by spray pyrolysis using a CNC-controlled system. The precursor solution was prepared by mixing titanium(diisopropoxide)bis(2,4-pentanedionate) 75% with ethanol 98% in a 1 : 19 volume ratio. After deposition, the films were crystallized by annealing in air at 500 °C for 20 minutes and allowed to cool naturally to room temperature.

The Sb_2Se_3 precursor layer was deposited by co-evaporation of high-purity elemental Sb and Se in a state-of-the-art co-evaporation system. The base pressure was maintained below 5×10^{-7} mbar. Effusion cells were heated to 550 °C for Sb and 230 °C for Se, while the substrate temperature was held at 270 °C to promote crystal formation. This process enables precise control of film thickness by adjusting the deposition time. The film composition and thickness were verified by X-ray fluorescence spectroscopy. For this study, all films were fabricated with a nominal thickness of $\sim$450 nm. Composition measurements consistently revealed a slight selenium excess (+5%), with Se accounting for approximately 65% of the atomic ratio. This Se-rich composition is beneficial, as it helps suppress the formation of selenium vacancies and promotes improved optoelectronic quality in the resulting films.[23]

2.2. Reactive annealing process

After deposition, the samples were subjected to reactive annealing treatment in a semi-confined environment to promote the

conversion of Sb_2Se_3 into SbSeI. Each sample was placed inside a borosilicate glass Petri dish, which provides partial confinement of the vapor-phase SbI_3 reactant. High-purity antimony(III) iodide (SbI_3 99.999%) powder was evenly distributed around the sample to enable homogeneous interaction during the reaction. The Petri dish assembly was then placed inside a high-pressure tubular furnace. To ensure oxygen-free conditions, the chamber was pump-purged three times with high-purity argon. After purging, argon was introduced to an initial pressure of 5.5 bar (absolute), corresponding to 4.5 bar gauge as measured using a pressure sensor (referenced to 1 atm). Annealing experiments were conducted at various temperatures and durations as described in the main manuscript. In all cases, the furnace was ramped at a constant rate of 10 °C min^{-1}, followed by isothermal holds at the target temperature. After annealing, the system was allowed to cool naturally to room temperature.

2.3. Characterization techniques

The thickness and composition of all Sb_2Se_3 precursor layers were determined by X-ray fluorescence (Fischerscope X-Ray XDAL 237 SSD, 50 kV, Ni10 filter), using calibrated standards. In contrast, no measurements were performed on the resulting SbSeI films, as their irregular surface morphology prevented reliable quantification with this technique, which requires flat and uniform films. Cross-sectional SEM-EDS line scans were used to assess the elemental distribution across representative samples. Morphological and structural characterization of the SbSeI samples was performed using SEM and XRD. SEM images were acquired using a Zeiss Auriga Series field-emission microscope operated at 5 kV. XRD measurements were conducted using a Bruker D8 Advance diffractometer in the Bragg–Brentano configuration, using Cu Kα radiation (λ = 1.54187 Å). Patterns were collected over a 2θ range of 10° to 80°, with a step size of 0.02°, and analysed using X'Pert HighScore software. The PDF patterns used for indexing are (01-075-1723) for SbSeI and (01-075-1462) for Sb_2Se_3.

Statistical analysis was performed using ImageJ for image-based measurements and OriginPro for data processing. For each sample, all visible columns within a selected region were measured until a sample size of $N > 300$ was reached to ensure statistical reliability. The resulting data were fitted to appropriate statistical distributions. Each fit was evaluated using the modified Kolmogorov–Smirnov (K–S) goodness-of-fit test, accompanied by Q–Q plots for visual verification of the model (Table S3 and Fig. S13–S24, SI).

3. Results and discussion

A schematic overview of the synthetic protocol is shown in Fig. 1A, which summarizes the main steps involved in the preparation of SbSeI films: precursor deposition (1), reaction assembly (2), and high-pressure reactive annealing (3). As schematically summarized in Fig. 1B and C, the morphological evolution with temperature is interpreted in terms of a shift in the dominant transport regime, from SbI_3 vapor diffusion at low temperatures to an increasing contribution of Se solid-state diffusion at higher temperatures. In all experiments, the SbI_3 charge was fixed at 50 mg to ensure a fair comparison across annealing conditions. Whether this mass is sufficient to saturate the volume of the Petri dish depends on the saturation vapor pressure of SbI_3, $P_{sat}(T)$, and the vessel volume $V \approx 43$ cm^3. Using the ideal gas law, the minimum mass required to saturate the volume at temperature T is estimated as follows:

$$m_{sat}(T) = \frac{P_{sat}(T) \cdot V \cdot M}{R \cdot T}$$

where M is the molar mass of SbI_3 (502.5 g·mol^{-1}), and R is the universal gas constant. This yields $m_{sat} \approx 16.3$ mg at 250 °C (523 K) and 60 mg at 300 °C (573 K). Therefore, the 50 mg charge is sufficient to saturate the volume at 250 °C but becomes subsaturated at 300 °C and above (the saturation values for all annealing setpoints are provided in the SI, Table S1). In practice, this means that the low-temperature regime operates near vapor saturation, while at higher temperatures the SbI_3 fully evaporates, but still maintains a SbI_3-rich atmosphere sufficient to sustain the reaction.

An additional factor is the slow vapor loss from the Petri dish to the cooler regions of the reactor (cold sides of the metallic tubular furnace). However, at elevated total pressures, the gas-phase diffusivity of SbI_3 decreases $D \propto 1/P_{tot}$, which effectively slows vapor transport and reduces loss to cold regions.

All syntheses at temperatures above 250 °C were carried out under intentionally sub-saturated SbI_3 vapor conditions, using a fixed 50 mg precursor mass. Despite the sub-saturation, conversion proceeded efficiently, suggesting that high vapor concentrations are not strictly necessary. The stoichiometric mass required for the reaction, given the volume of the Sb_2Se_3 precursor used, is less than 2 mg.

During exploratory experiments conducted at lower pressures in the 1–3 bar range, it was observed that extended treatments led to film degradation whenever no residual SbI_3 was present in the Petri dish upon completion of the reaction, *i.e.*, the reagent had been fully consumed or lost. The use of elevated pressure mitigates this issue by slowing SbI_3 vapor loss and helping to preserve an SbI_3 partial pressure above the equilibrium value required for SbSeI stability, even at high temperatures. This stabilizing effect creates a more controlled reaction environment and allows a more systematic investigation of the influence of temperature and annealing duration on the morphology and structural quality of the resulting SbSeI films. Notably, all experiments were initiated at an initial absolute pressure of 5.5 bar; and due to thermal expansion, the final pressure increased significantly with temperature, reaching up to ~8 bar at 450 °C.

3.1. Reaction-driven evolution of morphology and crystal structures

To investigate the effects of annealing time and temperature on structural and morphological evolution, selected SEM micrographs and XRD patterns are shown in Fig. 2. These images highlight the main differences occurring during the conversion

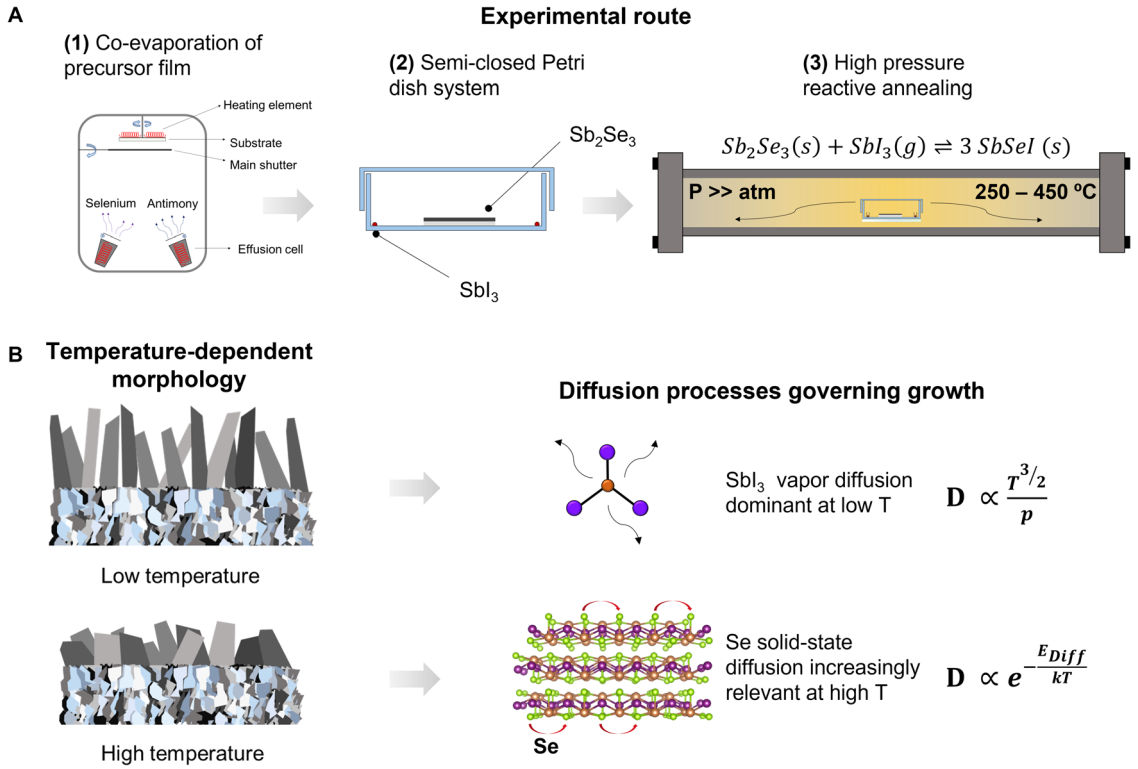

Fig. 1 Schematic representation of the synthesis protocol used in this study. (A) (1) Co-evaporation of antimony and selenium to form the Sb_2Se_3 precursor film. (2) Assembly of a semi-closed Petri dish system with SbI_3 powder and the precursor film. (3) High-pressure annealing ($p_0 \approx 4.5$ bar gauge) in a tubular furnace at 250–450 °C to promote the vapor–solid reaction forming SbSeI. (B) Summary of the two main approaches explored in this work: a morphological study (left), which reveals strong temperature dependence on the resulting nanostructures, and a kinetic study (right), highlighting the role of both gas-phase diffusion of SbI_3 and Se solid-state diffusion in controlling the growth mechanism.

of Sb_2Se_3 to SbSeI under different annealing conditions. A complete dataset, including all combinations of time–temperature, is provided in the SI (Table S2). Fig. 2A illustrates the thermal profiles used for the key experiments outlined here. A consistent ramp of 10 °C min^{-1} was applied to a set target temperature. These data are accompanied by the isothermal reaction at different temperatures for various durations. Two main regimes were explored: (i) a low-temperature (low-*T*) regime at 250 °C with (isothermal) reaction times from 1 to 45 minutes and (ii) a high-temperature (high-*T*) regime at 450 °C over the same time period. Additionally, three intermediate temperatures (300, 350, and 400 °C) were examined with a fixed dwell time of 5 minutes to effectively capture the transition between regimes. This experimental design enables the assessment of how thermal energy and processing time affect both reaction kinetics and film evolution, as well as whether changes in morphology correlate with reaction completeness.

Fig. 2B shows selected SEM micrographs illustrating the morphological evolution across different conditions at key points in the reaction process. Four representative images were chosen to exemplify the typical morphologies observed within the low-temperature and high-temperature regimes. The full series of SEM images is available in the SI (Fig. S1–S3) for a more comprehensive view. A clear contrast is observed between images 1 and 2, corresponding to the start and end of the low-*T* regime (250 °C isothermal reaction). Fig. 2B (image 1) displays the sample annealed for only 1 minute (after reaching the target temperature), and the reaction has just initiated, as evidenced by the appearance of short SbSeI needles on top of a clearly visible Sb_2Se_3 substrate (see Fig. S1 for a more detailed view). These data reveal that SbSeI nucleates as discrete islands on top of the substrate layer, suggesting a Volmer–Weber growth mode. From these islands, single needles emerge, suggesting that each needle originates from a localized nucleus rather than from a continuous SbSeI wetting layer. This nucleus-to-needle transition is a key morphological signature that supports a reaction-diffusion model (*vide infra*). Specifically, local interaction between Sb_2Se_3 and SbI_3 first produces compact SbSeI nuclei, after which anisotropic growth along the quasi-1D axis rapidly dominates. This image also confirms that the nucleation temperature of SbSeI is below 250 °C, consistent with TGA results of SbI_3 sublimating at 200 °C.[24] Cross-sectional SEM images (Fig. S4) confirmed that this initial transformation is limited to the surface. With prolonged annealing at 250 °C, both the population density and the length of the needles increase gradually. After 30 minutes, the substrate is no longer visible in top-view SEM (Fig. S1), with the final sample (Fig. 2B image 2) displaying the complete coverage of SbSeI needles.

To further investigate the effect of temperature, annealing was performed at 300, 350, and 400 °C for 5 minutes each. Representative SEM images are included in the SI (Fig. S2).

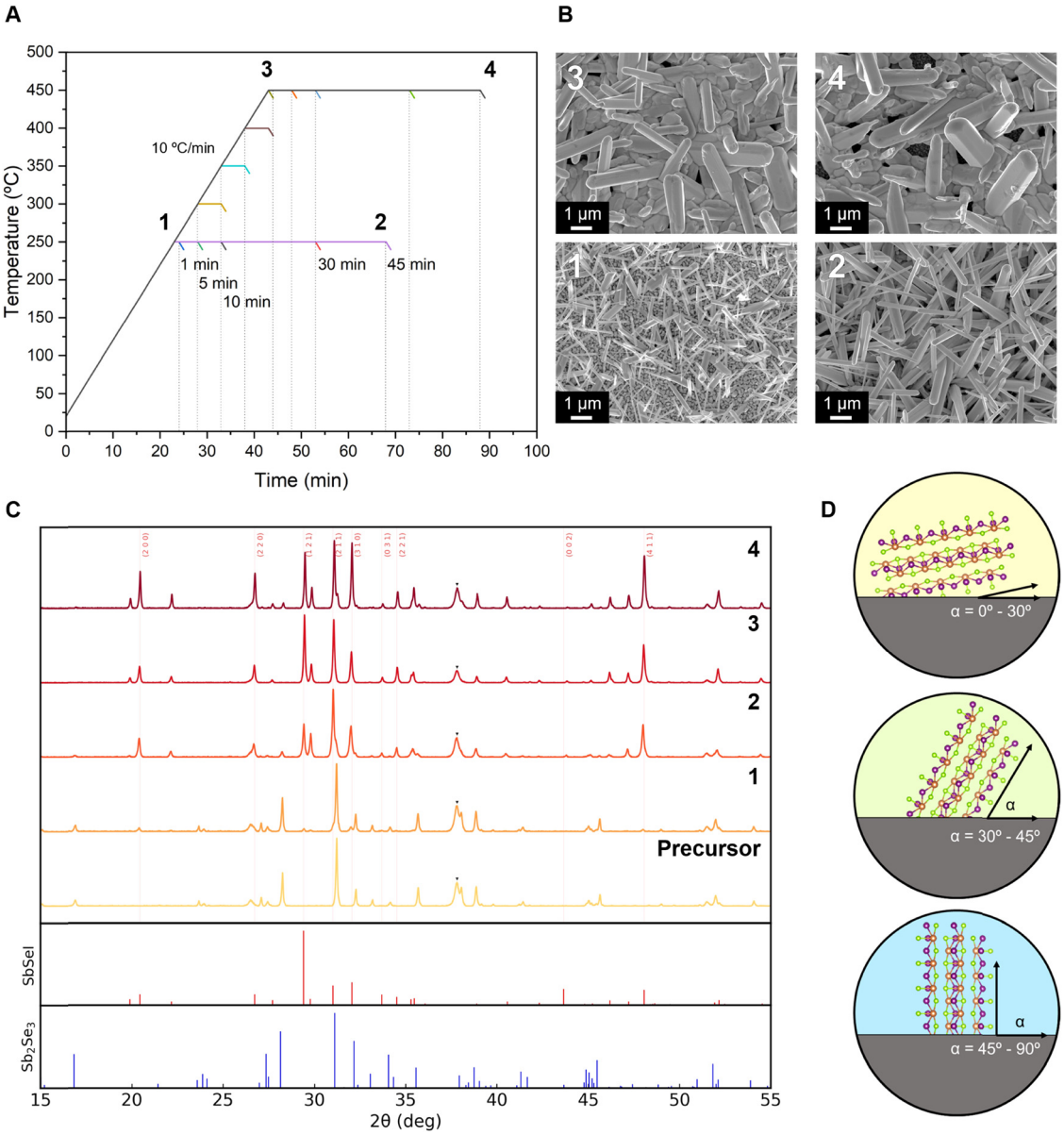

Fig. 2 (A) Thermal profile and annealing conditions. (B) SEM images showing morphological evolution under different conditions. (C) XRD patterns of the precursor and annealed samples. The PDF patterns for indexing are SbSeI (01-075-1723) and Sb_2Se_3 (01-075-1462). (D) Possible needle orientations with respect to the substrate obtained from the calculation of the texture coefficient.

Similarly, short annealing at 350 °C produces a clear morphological shift: the needles also become denser and longer. In contrast, as the temperature increases beyond 350 °C, the needle density decreases while their diameter increases, particularly at the base, indicating the onset of a different growth regime. At 450 °C, the morphology transitions into thick needles. A quantitative analysis of needle dimensions as a function of temperature in this transition regime is presented in Section 3.2.

Fig. 2B (images 3 and 4) shows the beginning and end of the high-*T* regime (450 °C isothermal anneal). The morphology changes only slightly from 1 to 45 min and is already similar to the 400 °C sample (Fig. S2). The main change in the grain size and needle thickness therefore occurs when moving from the low-*T* to the high-*T* regime and is largely insensitive to processing time, indicating that the morphological transition is essentially completed by ~400 °C. Further thermal input mainly affects structural metrics such as crystalline quality (FWHM), texture (TC), and grain size.

In Fig. 2B (image 3), a continuous layer with an appearance distinct from the Sb_2Se_3 precursor is observed around the needles. Cross-sectional EDS line scans collected across both the underlayer and individual needles confirm the presence of Sb, Se and I in both regions, supporting the assignment of this continuous layer as a converted SbSeI-rich underlayer. Together with XRD, these data indicate that high-temperature processing

promotes not only needle formation but also a more extensive background conversion prior to the later-stage thickening of the needles. In Fig. 2B (image 4; 450 °C, 45 min), some regions of the substrate become exposed, consistent with needle growth drawing material from this layer, locally thinning it and uncovering the underlying substrate.

The XRD patterns in Fig. 2C (corresponding to images 1–4) provide an overview of the phase evolution. Pattern 1 (image 1) is dominated by Sb_2Se_3, indicating minimal reaction progress, in agreement with SEM. By contrast, patterns 2 and 3 show an almost single SbSeI phase. The markedly different morphologies in images 2 and 4, despite similar phase purity, indicate distinct growth regimes. Finally, Fig. 2D illustrates possible needle orientations relative to the substrate. We quantify this using the texture coefficient, calculated from 14 representative peaks, which shows only a slight preferential orientation (Fig. S6). TC values above one for multiple ($hk1$) planes are consistent with a moderate population of tilted needles, as schematically indicated in green in Fig. 2D; this interpretation is also supported by the cross-sectional SEM images (Fig. S4), where inclined needle growth can be directly observed.

To evaluate the structural transformation during annealing, X-ray diffraction (XRD) measurements were performed. The full series of diffraction patterns is provided in the SI (Fig. S7–S9), while representative patterns are shown to highlight the main structural differences.

Fig. 3 includes a focused analysis of the XRD patterns (28° to 32°) across the three distinct temperature regimes: high (Fig. 3A, 450 °C), transition (Fig. 3B, 300–400 °C), and low (Fig. 3C, 250 °C). This angle region contains important reflections that permit the obtention of an estimation of the reaction completeness. Reaction progress, X, is qualitatively estimated from the bounded, reference intensity ratio (RIR) corrected peak areas of Sb_2Se_3 (r) and SbSeI (p) using the following equation $X = \frac{A_p}{A_p + \alpha A_r}$, where $\alpha = RIR_p/RIR_r$. Here, A_p and A_r correspond to the SbSeI (211) and Sb_2Se_3 (212) reflections, respectively. These reflections were selected because they correspond to the most intense peaks when the analysed phase is dominant, *i.e.*, at very short times (precursor phase) or very long times (final product). This choice simplifies peak deconvolution and area integration, enabling reliable extraction of the respective peak areas. This representation is useful for comparing trends across the dataset, but it should not be interpreted as an absolute conversion fraction because the intensities may also be affected by preferred orientation, overlap, and morphology-dependent scattering. Within these limitations, the low-T series follows an approximately linear dependence on sqrt(t), which is consistent with diffusion-limited reaction progress in this regime. The results of this analysis are shown graphically in Fig. 3D and allow for the visualization of reaction progress in different temperature regimes.

At 250 °C, the XRD patterns show a clear progression with time. For short annealing durations (1, 5, and 10 min), the dominant reflections belong to the precursor phase Sb_2Se_3, consistent with the limited morphological transformation

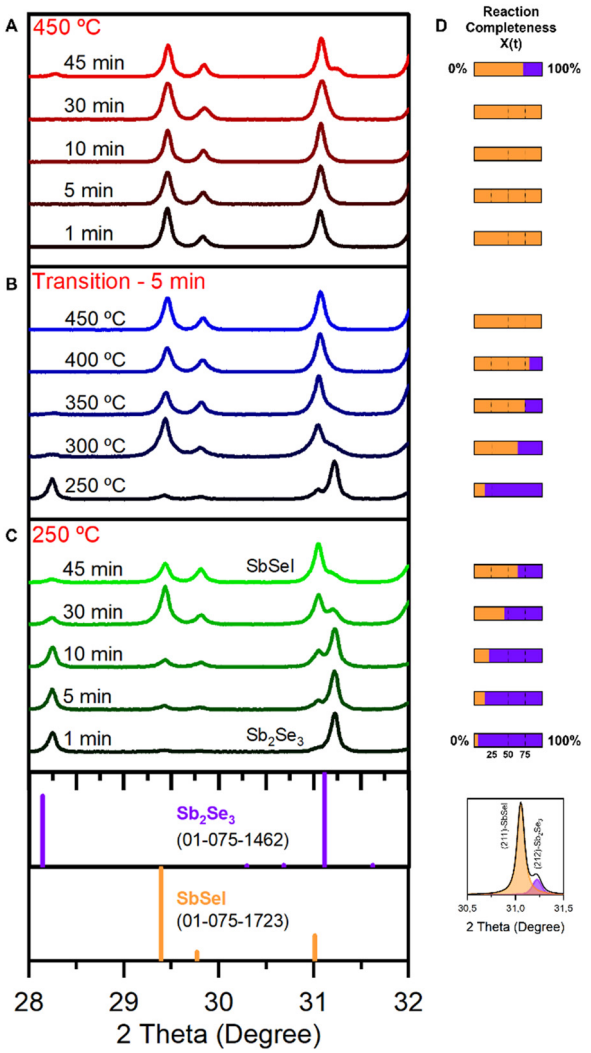

Fig. 3 Left: Detailed XRD patterns highlighting the main peak region (28°–32° 2θ), illustrating the phase transition across different annealing regimes (A: high temperature, B: transition regime, and C: low temperature). Right: Graphical representation of the reaction progress, derived from the bounded intensity ratio of the peaks within the 30.5°–31.5° region.

observed in SEM. After 30 minutes, the main peak corresponds to the SbSeI orthorhombic phase, although residual Sb_2Se_3 peaks persist. Even after 45 min, complete conversion is not achieved, indicating that the reaction remains kinetically hindered at this temperature and pressure. Given that the reaction proceeds far more efficiently at higher temperatures, long-duration low-temperature treatments are less practical.

Between 250 and 300 °C, the reaction shows a clear acceleration, shifting from an Sb_2Se_3-dominated phase to predominantly SbSeI. SEM observations (Fig. S2) corroborate this change, showing a strong increase in needle density, while the overall needle morphology remains largely unchanged. Between 300 and 400 °C, the reaction continues more gradually, and the morphological differences described above begin to emerge (Fig. S3).

Fig. 3A shows the high-T regime (450 °C) where the reaction evolution is substantially different from the other regimes. The XRD patterns in the high-T remain essentially unchanged between 1 and 30 minutes. This indicates that the conversion of Sb_2Se_3 into SbSeI is already complete before the system reaches the final setpoint of 450 °C. Indeed, as shown previously, annealing at 400 °C for just 5 minutes already results in almost fully formed SbSeI, confirming that the phase transition occurs during the heating ramp or very early in the dwell. An alternative strategy for accessing the high-temperature regime would be required to decouple it from the effects of slow heating, since with the present approach, early nucleation will inevitably influence the final morphology. Therefore, this high-temperature series primarily captures post-reaction processes such as structural rearrangement, grain growth, and preferred orientation. Notably, the stability of the SbSeI phase is preserved up to 30 minutes at 450 °C under these conditions. At the longest annealing time (*i.e.*, 45 min), signs of decomposition emerge, including the reappearance of Sb_2Se_3 peaks. We attribute this degradation to the significant depletion of SbI_3 vapor after extended high-temperature annealing, which causes a partial reversion (back reaction) to the precursor phase.

In addition, to assess the crystallinity of the synthesized thin films, the full width at half maximum (FWHM) of the main SbSeI diffraction peaks was analysed across all samples. After accounting for peak broadening due to overlapping phases (and weak signal intensity), a slight narrowing trend is observed with increased reaction time in both low- and high-T regimes (Fig. S10), indicating a moderate improvement in crystallinity with reaction time.

3.2. Growth kinetics and needle formation

To quantitatively assess SbSeI morphological changes across synthesis conditions, we performed a statistical analysis of needle thickness (width) extracted from SEM images. It should be noted that the needle thickness is systematically measured at the base or, when it is not clearly accessible, at the thickest observable section of the structure. This choice is motivated by the growth morphology, as material incorporation occurs preferentially near the root of the needles, making this region the more representative of their growth state. This consideration is particularly relevant in the low-T regime, where pronounced tapering is observed. At higher temperatures, the increased mass redistribution (discussed below) leads to more uniform needle geometries, reducing the sensitivity of the measurement to the exact location along the structures. Importantly, the resulting thickness distributions were found to be reproducible across different regions of the same sample and across repeated syntheses performed under the same nominal conditions, supporting the robustness of the observed statistical trends. Fig. 4 shows the evolution of the needle-thickness distributions as a function of processing conditions and time. Each regime yields a distinct statistical signature, providing insight into the growth kinetics. Two main distribution types are observed: Weibull (low-T) and lognormal (high-T).

The Weibull distribution is a two-parameter model for positive-valued quantities. Its survival function is:

$$S(x) = \exp\left[-\left(\frac{x}{\lambda}\right)^k\right]$$

With the corresponding hazard function:

$$h(x) = \frac{k}{\lambda}\left(\frac{x}{\lambda}\right)^{k-1}$$

Here, k is the shape parameter. Values of $k > 1$ imply that the stopping hazard increases with thickness; *i.e.*, conditional on having reached a thickness x, the probability that a needle stops growing per additional increment of thickness becomes larger as x increases. The scale parameter λ sets a characteristic thickness (since $F(\lambda) = 1 - e^{-1} \approx 0.63$, ~63% of values lie below λ).

In the present system, changes in k can be interpreted as changes in the degree of size-dependent growth limitation. At the earliest stage (Fig. 4A), the morphology is still sparse and growth is weakly constrained by impingement, leading to a distribution that deviates from the Weibull form. At longer times (Fig. 4B and C), the needle population density increases, and available free space becomes limited. The continued population in the first histogram bin at all processing times indicates that new needles keep nucleating heterogeneously throughout the process, rather than nucleation occurring only at early times. In this crowded regime, simultaneous growth promotes needle–needle impingement and competition for reagents. As a result, thicker needles, requiring more material flux and more space to continue growing, exhibit a higher stopping hazard. The observed increase of k with processing time indicates that this size-dependent limitation becomes progressively more pronounced.

In contrast, the high-temperature regime is well described by a lognormal thickness distribution. In this case, the histograms shift systematically to larger values, and the minimum needle thickness increases with temperature, indicating that the population of very thin needles progressively disappears.

A lognormal variable X is such that:

$$\ln X \sim N(\mu, \sigma^2)$$

Physically, this behaviour is consistent with multiplicative growth, where the thickness evolves through many small, independent percentage-like increments. The median thickness is $\exp(\mu)$, and the geometric standard deviation is $\exp(\sigma)$, controlled by the spread parameter σ.

The loss of counts in the low-thickness bins seen in Fig. 4E and F suggests a change in the nucleation/growth regime. Rather than continuous formation of new thin needles, the morphology points to a more homogeneous deposition background, visible as the continuous layer surrounding the needles in Fig. 4F (see also Fig. S3). In this scenario, the pre-formed needles act as preferential sinks for material redistribution, while the surrounding layer progressively feeds their thickening

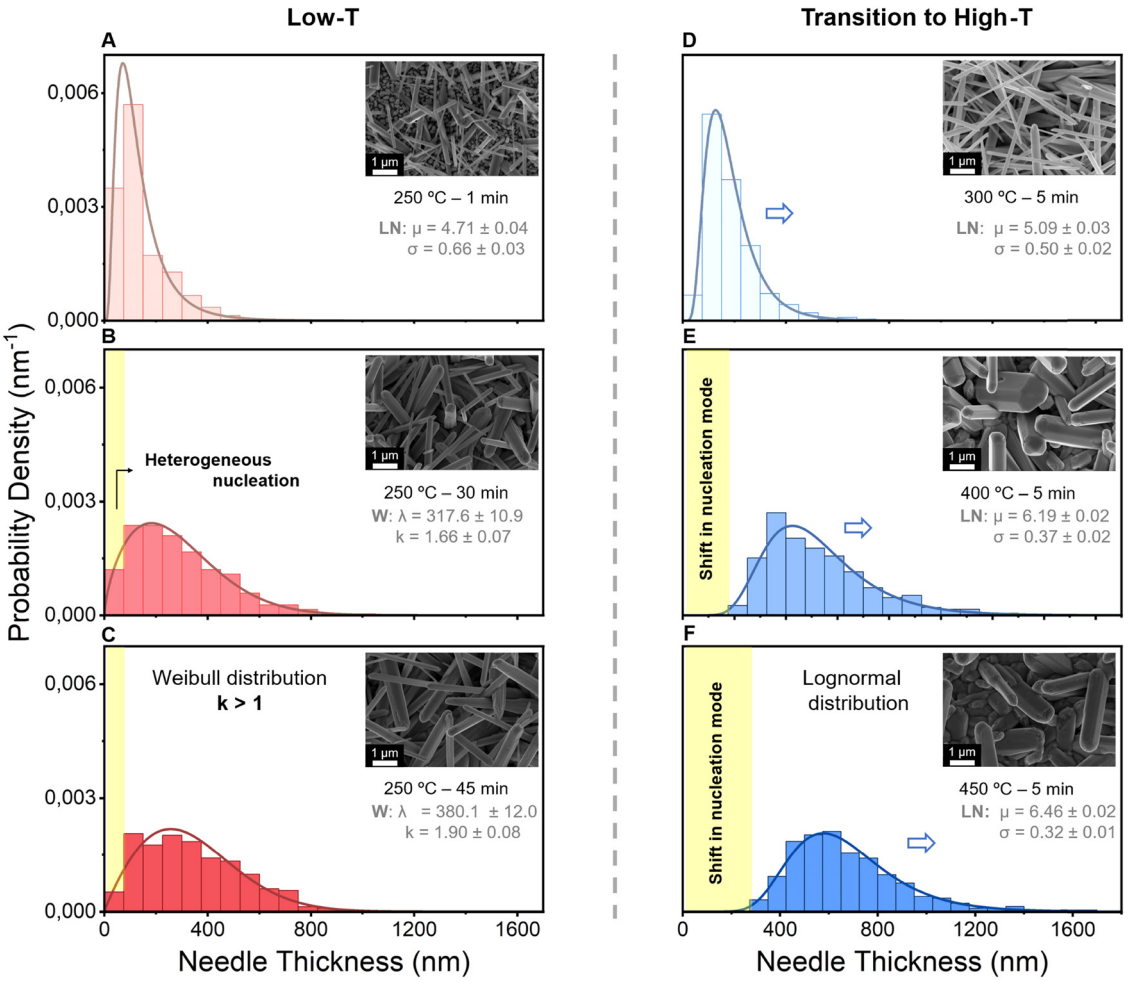

Fig. 4 Needle thickness distributions for SbSeI films synthesized under different annealing conditions. Panels A–C correspond to the low-temperature regime (250 °C). Panels D–F correspond to higher-temperature processes (300–450 °C). Each histogram is fitted with either a Weibull or lognormal distribution, as indicated. Insets show the representative SEM images of the corresponding morphology.

via coarsening, suggesting an Ostwald ripening process. This process naturally suppresses small features and amplifies size differences, leading to a lognormal distribution and, at long annealing times, to fewer, thicker, and more isolated needles. Consistently, Fig. 2B already shows regions where the FTO becomes exposed, indicating that the background layer locally thins as the mass is transferred to the growing needles.

Further insight into the growth mechanism is obtained from the evolution of the converted fraction (α), as approximated from XRD peak intensity ratios. In typical diffusion-limited systems, a square root dependence is inferred from the progression of a well-defined interface; here, the material grows as disconnected, high-aspect-ratio needles. As such, the XRD-derived ratio serves as an approximate metric to track conversion over time. It is also important to note that no strong preferential orientation was observed across the samples, making the use of peak intensity ratios valid for this purpose. The observed $\alpha \propto \sqrt{t}$ trend is linear at low temperatures, indicating diffusion-limited growth (Fig. S11). Since the reaction was already complete before reaching the high-T regime, no kinetic law is assigned to those conditions. Likewise, because kinetic laws are time-dependent, no kinetic law is assigned to the transition regime either.

The physical origin of this diffusion-limited behaviour may be deduced from a simplified reaction-diffusion model based on solid-state kinetics.[25] Fig. 5 shows a schematic representation of the proposed interpretation supported only by indirect evidence. After an initial period of local interaction between the Sb_2Se_3 substrate and SbI_3 vapor, the system can be approximated as comprising three regions: (A) the Sb_2Se_3 substrate, (B) the SbI_3 vapor phase, and (C) the growing SbSeI product. Two distinct interfaces are then defined: interface 1, between (A) and (C), and interface 2, between (B) and (C). For simplicity, it is assumed that Sb is available throughout the system, which is reasonable as it is supplied by both precursors. This framework is focused on rationalizing the main reaction ($Sb_2Se_3 + SbI_3 \rightarrow 3$ SbSeI) and the emergence of anisotropic needles. The subsequent coarsening of SbSeI at high temperatures may then be addressed qualitatively in terms of mass redistribution within the product layer. Growth at interface 1, between Sb_2Se_3 and

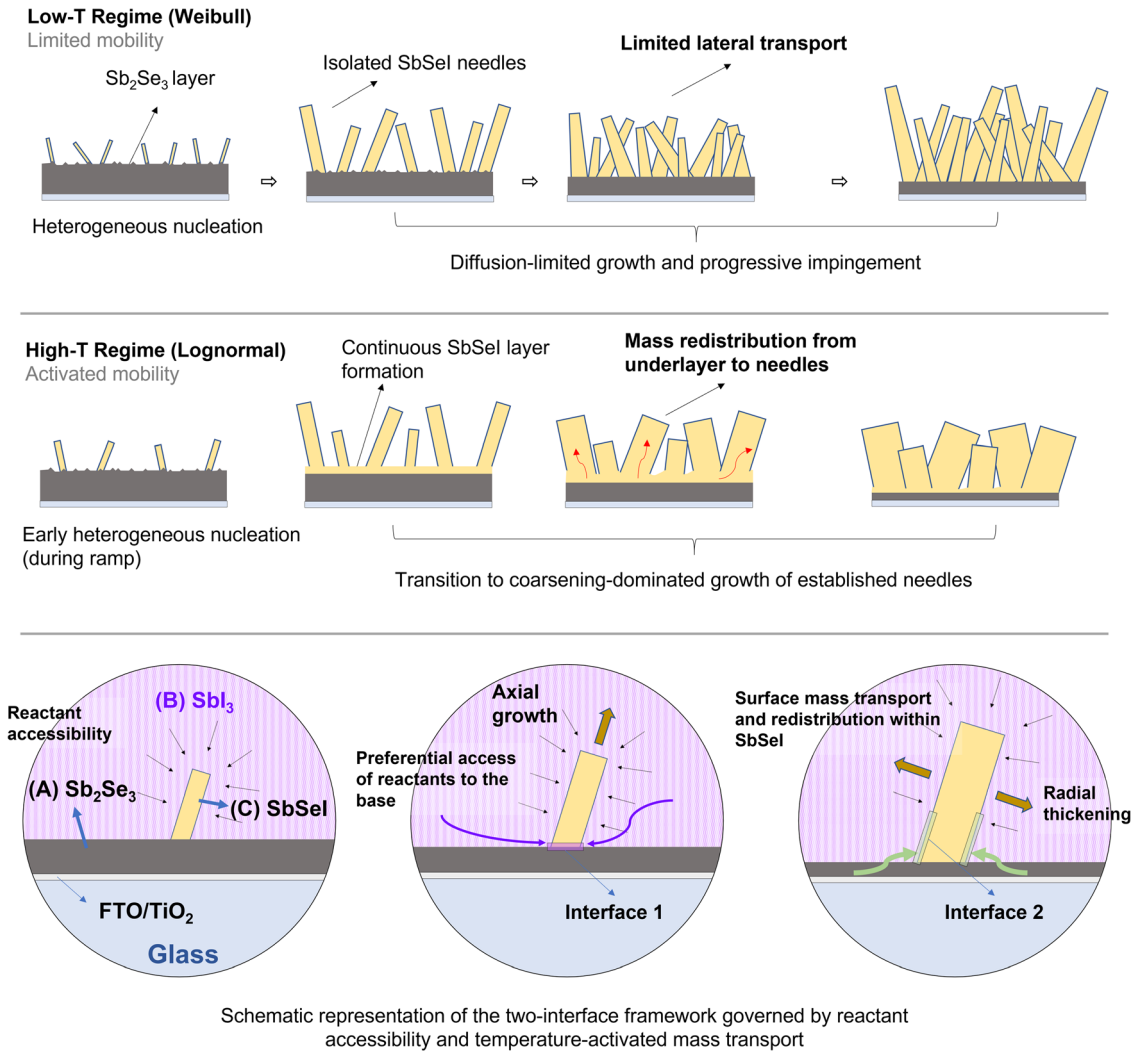

Fig. 5 Schematic representation of the two growth regimes identified in this work. Top row: the low-temperature regime with continuous heterogeneous nucleation and diffusion-limited conversion (A/B/C framework), leading to a dense forest of needles with a Weibull thickness distribution. Middle row: the high-temperature regime, where nucleation becomes temporally confined and rapid background conversion forms a SbSeI layer that subsequently feeds the coarsening of established needles, resulting in lognormal thickness statistics and thick isolated columns. Bottom row: schematic of the proposed diffusion-limited reaction model. Interface 1 (Sb_2Se_3/SbSeI) drives axial needle elongation *via* iodine-rich species vapor diffusion (purple arrows). Interface 2 (SbI_3/SbSeI) governs radial thickening (green arrows), which is confined to the needle base to highlight the limited selenium supply and restricted lateral growth.

SbSeI, is associated with the advance of the reaction front into the precursor and contributes primarily to the elongation of the needles. In the low-temperature regime, this axial growth is favoured because iodine-rich vapor species can sustain the reaction at the base of the needles, where the product remains in direct contact with the precursor. However, the approximately linear dependence of the reaction-progress metric with $\sqrt{t}$ in this regime suggests that the global conversion rate is limited by a diffusive process. A plausible origin of this limitation is the restricted transport of SbI_3 vapor under the combined low-temperature and high-pressure conditions, even though this vapor-phase transport remains the dominant channel sustaining growth. At the same time, selenium redistribution within the solid is expected to occur but to remain strongly hindered. As a result, radial propagation of the product and thickening away from the substrate region are limited, while local radial growth is mainly observed near the needle base, where slowly redistributed selenium can still be incorporated. This interpretation is consistent with the SEM observations, where the base of the needles is systematically thicker than the tip, indicating that material incorporation is kinetically favoured close to the substrate while radial development farther from the base remains restricted.

This anisotropic growth is also consistent with the crystal structure of SbSeI. As a quasi-one-dimensional material, SbSeI is expected to grow more readily along its covalently connected structural direction than across the less strongly bonded van der Waals sides. Although this argument does not by itself determine the rate-limiting step, it provides a thermodynamic and structural basis for why the available mass is preferentially

expressed as needle elongation rather than lateral widening under kinetically constrained conditions.[26]

As the temperature increases, the simple diffusion-limited picture identified at low temperatures becomes progressively less adequate, as the overall reaction rate increases and no clear kinetic law can be inferred. What remains clear, however, is that processes associated with interface 2, between the vapor phase and the SbSeI product, become increasingly relevant because atomic mobility within the converted layer improves. Under these conditions, selenium redistribution through the product becomes more efficient, facilitating access to the needle flanks and promoting lateral thickening. This effect is already suggested in the transition regime, where the first clear increase in needle diameter is observed. At still higher temperatures, the enhanced accessibility of iodine-rich species to the base region is accompanied by increasingly relevant selenium transport within the product, leading not only to faster overall conversion but also to substantial mass redistribution within the SbSeI layer. In this regime, the continuous SbSeI layer observed in Fig. 4F at intermediate stages can act as a local mass reservoir, progressively feeding the most stable needles and contributing to the pronounced thickening and partial disappearance of the background layer observed after long annealing times.

Prior studies of solid-state diffusion identify a critical temperature T_c separating the regimes of limited and activated surface mobility.[27] Empirically, T_c often scales with the material's melting temperature T_{melt}:

$$T_c/T_{melt} = 0.65–0.75.$$

SbSeI has a melting point near 460 °C, which places T_c in the range of 300–350 °C.[17] This matches well the temperature window where a marked increase in needle diameter is observed (Fig. S5). While this relationship should be taken as an empirical guideline rather than a strict proof, it is consistent with the morphological transition identified here. As atomic mobility becomes sufficiently activated for $T > T_c$, selenium redistribution within the SbSeI layer increasingly favours the thickening of the needles. In the high-temperature regime, where the system approaches the melting point more closely, this enhanced mobility is expected to promote stronger mass transfer towards the most stable crystal shapes, consistent with the formation of larger and thicker needles.

This empirical T_c estimate provides a physical rationale when lateral thickening becomes kinetically activated. However, it does not address the role of the Sb_2Se_3 precursor on transformation. Previous work has suggested that the transformation from Sb_2Se_3 to SbSeI may be topotactic.[20] A topotactic reaction implies a clear crystallographic relationship between the precursor and the product, such that specific directions or planes of the product remain quasi-parallel to those of the precursor and part of the underlying atomic skeleton (*e.g.*, sub-anion networks, chains, or layers) is preserved. Importantly, preservation of the macroscopic morphology is not a strict requirement. Therefore, the marked morphological evolution observed here, from a compact Sb_2Se_3 layer to a needle-like SbSeI film, does not contradict a topotactic transformation.[28]

Given that both Sb_2Se_3 and SbSeI are strongly anisotropic, quasi-1D materials built from Sb–Se ribbons, or chain-like motifs, it is natural to consider a local topochemical pathway in which the coordination within individual Sb_2Se_3 ribbons is reorganized upon iodine incorporation, yielding SbSeI domains structurally related to the precursor. Consistent with this picture, early-stage SEM images (Fig. S4) acquired at low temperatures and short reaction times show isolated SbSeI needles emerging from an otherwise continuous Sb_2Se_3 background. This morphology suggests that nucleation may be spatially selective, potentially occurring at specific sites where the local structure, orientation, or defects favour the anisotropic growth of SbSeI. While we cannot directly resolve such local crystallographic relationships with the present dataset, this interpretation offers a plausible working hypothesis that will be explored in future works.

4. Conclusions

This study identifies the key parameters that govern the growth, morphology, and crystallinity of SbSeI thin films synthesized *via* reactive annealing. Notably, we identify two distinct statistical distributions of grain size, each associated with a different synthesis regime. These findings support a solid formation model that explains how processing parameters affect growth dynamics. According to our model, columnar structures originate at the substrate interface *via* a kinetically limited process governed by SbI_3 vapor diffusion and solid-state selenium diffusion. A critical temperature threshold is identified, above which atomic mobility becomes sufficiently active to promote significant lateral growth, resulting in the formation of large, well-defined needles.

A clear distinction between low- and high-temperature regimes is established. At low temperatures, continuous heterogeneous nucleation combined with limited lateral diffusion yields densely packed, high-aspect-ratio needles. In contrast, access to higher temperatures shifts the nucleation mode and promotes multiplicative growth and coarsening of existing structures. When coupled with enhanced lateral diffusion, this leads to the formation of thicker, more crystalline needles. Despite the improved control over morphology and crystallinity, no strong preferential orientation was achieved under the tested conditions. Further studies are needed to understand and manipulate the crystallographic alignment of SbSeI films, an essential step toward optimizing performance in anisotropic optoelectronic applications.

The heating ramp rate emerges as a major limitation in accessing purely high-temperature regimes. The relatively slow ramp (10 °C min^{-1}) used in this work causes the reaction to initiate and largely complete at lower temperatures, limiting the ability to probe uninhibited high-temperature growth. In addition, this ramp appears to define a broad nucleation window, such that needles that nucleate early experience

substantially more growth time and different local conditions than those that nucleate later. In the low-temperature regime, this likely contributes to a wide diameter distribution that includes both very thin and comparatively thick needles, whereas a narrower distribution may be desirable for improved morphological uniformity. To overcome these limitations, the implementation of rapid thermal processing (RTP) is proposed for future studies, enabling sharper control over reaction onset, a more confined nucleation window, and better access to high-temperature growth pathways.

Importantly, this work has demonstrated that using elevated pressures proves beneficial by suppressing the SbI_3 vapor loss through reduced gas-phase diffusivity. This stabilization allows for longer processing times, which correlates with increased crystallite size and improved structural order, as evidenced by narrower XRD peak widths.

Overall, the insights presented here offer a foundation for tailoring synthesis parameters to engineer desired SbSeI film morphologies. These principles may also extend to the broader class of quasi-one-dimensional materials, where diffusion-limited kinetics and anisotropic growth play critical roles.

Author contributions

Alejandro Navarro: writing – original draft, methodology, investigation, formal analysis, and conceptualization. Ivan Caño: methodology, investigation, and review and editing. David Rovira: methodology, investigation, and review and editing. Alex Jimenez: investigation and review and editing. Gabriel Aygur: investigation and conceptualization. Joaquim Puigdollers: resources and funding acquisition. Joel Van Embden: writing – review and editing, conceptualization, and validation. Edgardo Saucedo: review and editing, resources, funding acquisition, and supervision.

Conflicts of interest

There are no conflicts to declare.

Data availability

All data generated and/or analysed during this study are available on Zenodo. DOI: https://doi.org/10.5281/zenodo.18032939. Full URL: https://doi.org/10.5281/zenodo.18032939. Any additional data shown in the supplementary information (SI) are included within the supplementary information file(s) of this article. Supplementary information is available. See DOI: https://doi.org/10.1039/d6ma00048g.

Acknowledgements

This research has received funding from the European Union H2020 Framework Program under the SENSATE project: Low-dimensional semiconductors for optically tunable solar harvesters (grant agreement number 866018) and the Renew-PV European COST action (CA21148). E.S. and J.P. acknowledge financial support of the Spanish Ministry of Science and Innovation from the CURIO-CITY project (PID2023-148976OB-C41). E.S. and A.J.A. acknowledge funding from the MICINN project ACT-FAST (PCI2023-145971-2) and from the CETP-Partnership Program 2022. This work was part of Maria de Maetzu Units of Excellence Programme CEX2023 001300-M, funded by MCIN/AEI/10.13039/501100011033. A.N. acknowledges the Spanish Ministry of Science and Innovation for his FPI PhD grant (PRE-2021-098293). E.S. acknowledges the ICREA Academia program. The author gratefully acknowledges Mykhailo Kolstov, whose discussions during a secondment in Tallinn helped shape the initial ideas behind this work.

References

1 S. Farooq, T. Feeney, J. O. Mendes, V. Krishnamurthi, S. Walia, E. Della Gaspera and J. Van Embden, High Gain Solution-Processed Carbon-Free BiSI Chalcohalide Thin Film Photodetectors, *Adv. Funct. Mater.*, 2021, **31**(52), 2104788, DOI: 10.1002/adfm.202104788.

2 D. Tiwari, F. Cardoso-Delgado, D. Alibhai, M. Mombrú and D. J. Fermín, Photovoltaic Performance of Phase-Pure Orthorhombic BiSI Thin-Films, *ACS Appl. Energy Mater.*, 2019, **2**(5), 3878–3885, DOI: 10.1021/acsaem.9b00544.

3 R. Nie and S. I. Seok, Efficient Antimony-Based Solar Cells by Enhanced Charge Transfer, *Small Methods*, 2020, **4**(2), 1900698, DOI: 10.1002/smtd.201900698.

4 B. Peng, K. Xu, H. Zhang, Z. Ning, H. Shao, G. Ni, J. Li, Y. Zhu, H. Zhu and C. M. Soukoulis, 1D SbSeI, SbSI, and SbSBr With High Stability and Novel Properties for Microelectronic, Optoelectronic, and Thermoelectric Applications, *Adv. Theory Simul.*, 2018, **1**(1), 1700005, DOI: 10.1002/adts.201700005.

5 G. Peng, H. Lu, Y. Liu and D. Fan, The Construction of a Single-Crystalline SbSI Nanorod Array–WO_3 Heterostructure Photoanode for High PEC Performance, *Chem. Commun.*, 2021, **57**(3), 335–338, DOI: 10.1039/D0CC06148D.

6 M. C. Asensio and M. Batzill, Interfaces and Heterostructures of van der Waals Materials, *J. Phys.: Condens. Matter*, 2016, **28**(49), 490301, DOI: 10.1088/0953-8984/28/49/490301.

7 A. Eftekhari, Molybdenum Diselenide (MoSe 2) for Energy Storage, Catalysis, and Optoelectronics, *Appl. Mater. Today*, 2017, **8**, 1–17, DOI: 10.1016/j.apmt.2017.01.006.

8 J. Otavio Mendes, A. Merenda, K. Wilson, A. Fraser Lee, E. Della Gaspera and J. Van Embden, Substrate Morphology Directs (001) Sb_2 Se_3 Thin Film Growth by Crystallographic Orientation Filtering, *Small*, 2023, 2302721, DOI: 10.1002/smll.202302721.

9 Y. Zhou, L. Wang, S. Chen, S. Qin, X. Liu, J. Chen, D.-J. Xue, M. Luo, Y. Cao, Y. Cheng, E. H. Sargent and J. Tang, Thin-Film Sb2Se3 Photovoltaics with Oriented One-Dimensional Ribbons and Benign Grain Boundaries, *Nat. Photonics*, 2015, **9**(6), 409–415, DOI: 10.1038/nphoton.2015.78.

10 Z. Duan, X. Liang, Y. Feng, H. Ma, B. Liang, Y. Wang, S. Luo, S. Wang, R. E. I. Schropp, Y. Mai and Z. Li, Sb_2 Se_3 Thin-Film Solar Cells Exceeding 10% Power Conversion Efficiency Enabled by Injection Vapor Deposition Technology, *Adv. Mater.*, 2022, **34**(30), 2202969, DOI: 10.1002/adma.202202969.

11 X. Chen, B. Che, Y. Zhao, S. Wang, H. Li, J. Gong, G. Chen, T. Chen, X. Xiao and J. Li, Solvent-Assisted Hydrothermal Deposition Approach for Highly-Efficient Sb_2 $(S,Se)_3$ Thin-Film Solar Cells, *Adv. Energy Mater.*, 2023, **13**(21), 2300391, DOI: 10.1002/aenm.202300391.

12 I. Caño, P. Vidal-Fuentes, L. Calvo-Barrio, X. Alcobé, J. M. Asensi, S. Giraldo, Y. Sánchez, Z. Jehl, M. Placidi, J. Puigdollers, V. Izquierdo-Roca and E. Saucedo, Does Sb_2 Se_3 Admit Nonstoichiometric Conditions? How Modifying the Overall Se Content Affects the Structural, Optical, and Optoelectronic Properties of Sb_2 Se_3 Thin Films, *ACS Appl. Mater. Interfaces*, 2022, **14**(9), 11222–11234, DOI: 10.1021/acsami.1c20764.

13 I. Caño, A. Navarro-Güell, E. Maggi, A. Gon Medaille, D. Rovira, A. Jimenez-Arguijo, O. Segura, A. Torrens, M. Jimenez, C. López, P. Benítez, C. Cazorla, Z. Jehl, Y. Gong, J. Asensi, L. Calvo-Barrio, L. Soler, J. Llorca, J. Tamarit, B. Galiana, M. Dimitrievska, N. Ruiz-Marín, H. Z. Chun, L. Wong, J. Puigdollers, M. Placidi and E. Saucedo, Ribbons of Light: Emerging (Sb,Bi)(S,Se)(Br,I) van der Waals Chalcohalides for Next-Generation Energy Applications, *Small*, 2025, e05430, DOI: 10.1002/smll.202505430.

14 D. Rovira, I. Caño, C. López, A. Navarro-Güell, J. M. Asensi, L. Calvo-Barrio, L. Garcia-Carreras, X. Alcobe, L. Cerqueira, V. Corregidor, Y. Sanchez, S. Lanzalaco, A. Jimenez-Arguijo, O. El Khouja, J. W. Turnley, R. Agrawal, C. Cazorla, J. Puigdollers and E. Saucedo, Molecular Ink-Based Synthesis of $Bi(S_zSe_{1-z})(I_xBr_{1-x})$ Solid Solutions as Tuneable Materials for Sustainable Energy Applications, *Small Methods*, 2025, e01723, DOI: 10.1002/smtd.202501723.

15 U. V. Ghorpade, M. P. Suryawanshi, M. A. Green, T. Wu, X. Hao and K. M. Ryan, Emerging Chalcohalide Materials for Energy Applications, *Chem. Rev.*, 2023, **123**(1), 327–378, DOI: 10.1021/acs.chemrev.2c00422.

16 R. S. Nielsen, Á. L. Álvarez, A. G. Medaille, I. Caño, A. Navarro-Güell, C. L. Álvarez, C. Cazorla, D. R. Ferrer, Z. J. Li-Kao, E. Saucedo and M. Dimitrievska, Parallel Exploration of the Optoelectronic Properties of (Sb,Bi)(S,Se)(Br,I) Chalcohalides, *J. Mater. Chem. A*, 2025, **13**(37), 31727–31739, DOI: 10.1039/D5TA05011A.

17 A. C. Wibowo, C. D. Malliakas, Z. Liu, A. Peters John., M. Sebastian, D. Y. Chung, B. W. Wessels and M. G. Kanatzidis, Photoconductivity in the Chalcohalide Semiconductor, SbSeI: A New Candidate for Hard Radiation Detection, *Inorg. Chem.*, 2013, **52**(12), 7045–7050, DOI: 10.1021/ic401086r.

18 M. Nowak, B. Kauch, P. Szperlich, M. Jesionek, M. Kępińska, Ł. Bober, J. Szala, G. Moskal, T. Rzychoń and D. Stróż, Sonochemical Preparation of SbSeI Gel, *Ultrason. Sonochem.*, 2009, **16**(4), 546–551, DOI: 10.1016/j.ultsonch.2009.01.003.

19 Y. C. Choi and K.-W. Jung, One-Step Solution Deposition of Antimony Selenoiodide Films *via* Precursor Engineering for Lead-Free Solar Cell Applications, *Nanomaterials*, 2021, **11**(12), 3206, DOI: 10.3390/nano11123206.

20 S. K. Balakrishnan, P. C. Parambil and E. Edri, Mechanistic Insight into the Topotactic Transformation of Trichalcogenides to Chalcohalides, *Chem. Mater.*, 2022, **34**(7), 3468–3478, DOI: 10.1021/acs.chemmater.2c00306.

21 M. Dolcet Sadurni, K. Timmo, V. Mikli, O. Volobujeva, I. Mengü, J. Krustok, M. Grossberg-Kuusk and M. Kauk-Kuusik, Preparation and Characterization of SbSeI Thin Films, *J. Sci. Adv. Mater. Devices*, 2024, **9**(1), 100664, DOI: 10.1016/j.jsamd.2023.100664.

22 R. Nie, M. Hu, A. M. Risqi, Z. Li and S. I. Seok, Efficient and Stable Antimony Selenoiodide Solar Cells, *Adv. Sci.*, 2021, **8**(8), 2003172, DOI: 10.1002/advs.202003172.

23 P. Vidal-Fuentes, M. Placidi, Y. Sánchez, I. Becerril-Romero, J. Andrade-Arvizu, Z. Jehl, A. Pérez-Rodríguez, V. Izquierdo-Roca and E. Saucedo, Efficient Se-Rich Sb_2 Se_3/CdS Planar Heterojunction Solar Cells by Sequential Processing: Control and Influence of Se Content, *Sol. RRL*, 2020, **4**(7), 2000141, DOI: 10.1002/solr.202000141.

24 I. Caño, A. Navarro-Güell, E. Maggi, M. Barrio, J.-L. Tamarit, S. Svatek, E. Antolín, S. Yan, E. Barrena, B. Galiana, M. Placidi, J. Puigdollers and E. Saucedo, SbSeI and SbSeBr Micro-Columnar Solar Cells by a Novel High Pressure-Based Synthesis Process, *J. Mater. Chem. A*, 2023, **11**(33), 17616–17627, DOI: 10.1039/d3ta03179a.

25 V. I. Dybkov, *Reaction Diffusion and Solid Chemical Kinetics*, The IPMS Publications, Kyiv, 2002.

26 I. V. Markov, Crystal Growth for Beginners: Fundamentals of Nucleation, *Crystal Growth and Epitaxy*, World Scientific, New Jersey, 3rd edn, 2016.

27 E. Seebauer, Estimating Surface Diffusion Coefficients, *Prog. Surf. Sci.*, 1995, **49**(3), 265–330, DOI: 10.1016/0079-6816(95)00039-2.

28 J. Günter and H.-R. Ostwald, Attempt to a Systematic Classification of Topotactic Reactions, *Bull. Inst. Chem. Res., Kyoto Univ.*, 1975, **53**(2), 249–255.